Proceedings of FEDSM99
3rd ASME/JSME Joint Fluids Engineering Conference
July 18-23, 1999, San Francisco, California, USA

FEDSM99-7106

FORMATION OF DROPLETS IN MICROSCALE JETTING DEVICES

Igor D. Aleinov, Elbridge Gerry Puckett, Mark M. Sussman
Mathematics Department
University of California, Davis 95616
Email: aleinov@math.ucdavis.edu, egp@math.ucdavis.edu, sussman@math.ucdavis.edu

1 INTRODUCTION

We present the results of a computational study of the formation of droplets in microscale jetting devices. These devices are commonly used in applications where small size and accurate flow volume control are essential. It is currently possible to produce drops of fluid with diameters of 25-100 μm and volumes of 10 picoliters to 0.5 nanoliters at rates of up to 4,000 drops per second. In addition to ink-jet printing, applications include dispensing solder in microelectronics manufacturing processes (Bernardini et al., 1991), biomedical procedures and equipment (e.g., dye-assisted laser surgery), medical diagnostics manufacturing (e.g., printing DNA strands), micro-optics manufacturing, macro flow control, IC thermal management, micro-mixing and dispensing small amounts of chemicals in neuroscience research (Hayes et al., 1993; Wallace et al., 1989).

One of the features which is common to virtually all microscale jetting devices is that under most operating conditions the jet rarely consists of a single drop. Typically, the lead drop exits the nozzle of the device with a tail, which subsequently breaks off from the main drop. This tail then undergoes a Rayleigh capillary instability, breaking up into two or more "satellite droplets". These satellite droplets are typically smaller and have a lower velocity than the lead drop. In some instances two or more satellites will coalesce to form a smaller number of satellites, resulting in fewer satellite drops striking the target surface. Since it is often the case that the satellites have a different trajectory than the lead drop, their presence leads to quality control problems, such as loss of image resolution in ink jet printing applications.

We have developed a numerical method which is capable of modeling the entire jetting process; from the application of a time dependent pressure or velocity pulse at the inflow boundary of the nozzle, through the formation of the lead and satellite droplets, to the eventual coalescence of some or all of the satellite droplets. This numerical method is based on modeling solutions of the Navier-Stokes equations for two phase flow in domains with complex geometry. Our method is capable of accurately modeling flows which are characterized by a high density ratio between the two phases (e.g., 1000:1) and for which surface tension forces are a dominant feature of the flow.

2 GOVERNING EQUATIONS

We solve the following equations for incompressible two-phase flow:

$$\frac{\partial \vec{u}}{\partial t} + (\vec{u} \cdot \nabla)\vec{u} = -\frac{\nabla p}{\rho} + \frac{\nabla \cdot 2\mu\tau}{\rho} - \frac{\gamma\kappa\nabla H}{\rho} \tag{1}$$

$$\nabla \cdot \vec{u} = 0 \tag{2}$$

$$\frac{\partial \phi}{\partial t} + (\vec{u} \cdot \nabla)\phi = 0 \tag{3}$$

$$\frac{\partial F}{\partial t} + (\vec{u} \cdot \nabla)F = 0. \tag{4}$$

The above formulation is the level set formulation for multi-fluid flow (Sussman et al., 1994; Chang et al., 1996). It is shown (Chang et al., 1996) that weak solutions of (1) satisfy the free surface jump conditions,

$$(2\mu^l\tau^l - 2\mu^g\tau^g) \cdot \vec{n} = (p^l - p^g + \gamma\kappa)\vec{n} \tag{5}$$

where $\vec{n}$ is the outward normal drawn from the gas to the liquid and κ is the mean curvature.

The provisional variable ϕ represents the signed distance to the free surface. The variable F represents the volume fraction of liquid contained in any one computational cell. The density $\rho(\phi)$, viscosity $\mu(\phi)$, and Heaviside function $H(\phi)$ jump across the free surface (where ϕ changes sign). γ is the surface tension coefficient.

In order to solve (1), we use a variable density projection method (Bell and Marcus, 1992) which is a generalization of the constant density projection method (Bell et al., 1989). Firstly, one can rewrite (1) in the following form,

$$\vec{W}_d + \nabla p/\rho = \vec{W} \tag{6}$$

where W_d represents $\frac{\partial \vec{u}}{\partial t}$ and $\vec{W}$ represents,

$$-(\vec{u}\cdot\nabla)\vec{u} + \frac{\nabla\cdot 2\mu\tau}{\rho} - \frac{\gamma\kappa\nabla H}{\rho}. \tag{7}$$

After taking the divergence of both sides of (6), we use the continuity equation in order to set $\nabla\cdot\vec{W}_d = 0$, thus resulting in the equation for the pressure field:

$$\nabla\cdot\frac{\nabla p}{\rho} = \nabla\cdot\vec{W}. \tag{8}$$

. Once the pressure field p is determined from (8), one can then update $\vec{W}_d$ as

$$\vec{W}_d = \vec{W} - \nabla p/\rho.$$

The procedure of decomposing $\vec{W}$ into the two parts $\vec{W}_d$ and $\nabla p/\rho$ is called a projection since the set of divergence free vector fields and the set of gradient fields are orthogonal complements of each other when using a density weighted norm. We shall denote the projection operator as:

$$\vec{W}_d = P_\rho(\vec{W}).$$

.

The resulting equations to be solved now, when written in terms of the projection operator, are

$$\begin{aligned}\frac{\partial\vec{u}}{\partial t} &= P_\rho(-(\vec{u}\cdot\nabla)\vec{u} + \frac{\nabla\cdot 2\mu\tau}{\rho} - \frac{\gamma\kappa\nabla H}{\rho})\\ \frac{\partial\phi}{\partial t} &+(\vec{u}\cdot\nabla)\phi = 0\\ \frac{\partial F}{\partial t} &+(\vec{u}\cdot\nabla)F = 0.\end{aligned}$$

3 PROJECTION METHOD FOR GENERAL GEOMETRIES

In (8) we solve for the pressure with the condition that

$$\vec{W}_d\cdot\boldsymbol{n} = 0 \qquad \boldsymbol{x}\in\partial\Omega$$

where $\partial\Omega$ represents the boundary of some general geometry such as an ink-jet nozzle. In other words, we specify Neumann boundary conditions:

$$\frac{\nabla p}{\rho}\cdot\boldsymbol{n} = \vec{W}\cdot\boldsymbol{n} \qquad \boldsymbol{x}\in\partial\Omega \tag{9}$$

Explicitly enforcing (9) can be very difficult computationally; especially for complex geometries in three dimensions. For example, in a finite element implementation, there is the problem of remeshing if the geometry moves (e.g. a piston). Instead of solving (8) just in Ω with the boundary conditions specified by (9), we instead solve

$$\nabla\cdot H(\psi)\frac{\nabla p}{\rho} = \nabla\cdot H(\psi)\vec{W} \tag{10}$$

where ψ is a second level set function which is negative within solid bodies. The zero level set of ψ represents the boundary $\partial\Omega$. It can be shown that the weak solutions of (10) satisfy (9). Thus, the computational domain can be a rectangular domain, but the embedded boundary can be very complex.

4 COUPLED LEVEL SET VOLUME OF FLUID ADVECTION ALGORITHM

The location of the fluid interface is advanced in time using a coupled level set volume of fluid algorithm (Sussman and Puckett, 1998). In this algorithm the flux of each fluid across cell edges during a time step is computed from a second-order accurate, piecewise linear approximation to the interface. This representation of the interface is constructed from the volume fraction of each fluid in each cell at the current time step and the unit normal to the interface obtained from the level set function at that time step. The volume fractions in each cell at the new time step are computed using a conservative finite difference update, while a provisional level set function at the new time step is obtained by solving an advection equation for the level set function. This information at the new time step is used to obtain a piecewise linear approximation to the interface at the new time, which in turn is used to construct a distance function (i.e., the level set function) at the new time. This

distance function is then used to compute the unit normal and curvature of the interface. This information is used to compute the surface tension forces and the volume fluxes at the next time step.

4.1 Time Discretization

To advance the solution in time, we employ a variation of the time discretization used by Bell, Colella, and Glaz (Bell et al., 1989). It is a two-step algorithm. First we create a temporary velocity $\vec{u}^*$ by advancing the solution using the governing equations but ignoring the divergence constraint.

$$\vec{u}^* = \vec{u}^n + \Delta t \left(-\vec{u} \cdot \nabla \vec{u}^{n+\frac{1}{2}} - \frac{\nabla p^{n-\frac{1}{2}}}{\rho^{n+1/2}} - \frac{\frac{1}{2}\nabla \cdot (2\mu^{n+1/2}(\tau^n + \tau^*))}{\rho^{n+1/2}} - \frac{\gamma \kappa^{n+1/2} \nabla H}{\rho^{n+1/2}} \right) \quad (11)$$

where τ^n is the stress tensor evaluated using velocity $\vec{u}^n$ and τ^* is the stress tensor evaluated using velocity $\vec{u}^*$. Equation (11) therefore requires the solution of a linear system whose form depends on the form of the stress tensor. We then enforce the incompressibility constraint and update the pressure gradient by using the discrete projection operator $P_\rho^{discrete}$.

$$\vec{u}^{n+1} = P_\rho^{discrete}(\vec{u}^*) \quad (12)$$

$$\frac{\nabla p^{n+\frac{1}{2}}}{\rho^{n+\frac{1}{2}}} = (I - P_\rho^{discrete})(\vec{u}^*) + \frac{\nabla p^{n-\frac{1}{2}}}{\rho^{n+\frac{1}{2}}} \quad (13)$$

5 RAYLEIGH CAPILLARY INSTABILITY

When a droplet is ejected from an ink-jet device, typically a long cylindrical tail follows behind (see Figure 2). The number of satellite drops that appear behind the lead drop depend on the length of the tail, it's diameter, viscosity of the fluid, surface tension, among many other factors. The driving force that cause the tail to break-up into droplets is due to surface tension driven Rayleigh Capillary instability (Bechtel et al., 1995; Rayleigh, 1878; Wallace, 1993). In order for a numerical method to effectively predict jetting phenomena, it should converge to the exact solution under grid refinement when applied to these class of problems.

We consider an initially perturbed cylindrical column of water in air. The shape of the initial interface is,

$$r(z) = r_0 + \epsilon \cos(2\pi z/\lambda).$$

Table 1. Convergence study using the CLS algorithm for the capillary instability problem. All data in terms of dimensionless parameters. $t = 80.0$, $\mu_l/\mu_g = 64$, $\rho_l/\rho_g = 816$.

grid	E(interface)	$E_{u,L1}$	$E_{u,\max}$
16x32	N/A	N/A	N/A
32x64	36.88	268.7	0.064
64x128	21.13	167.5	0.050
128x256	8.14	94.2	0.034

We compute on an axisymmetric domain $\Omega = \{(r,z)|0 \leq r \leq \lambda/4 \text{ and } 0 \leq z \leq \lambda/2\}$. Symmetric boundary conditions are enforced at $r = 0$, $z = 0$ and $z = \lambda/2$. Outflow boundary conditions are enforced at $r = \lambda/4$. The relevant parameters for our test problem are $r_0 = 6.52$ microns, $\epsilon = 1.3$ microns, $\lambda = 60$ microns, $\mu_l = 1.138 \times 10^{-2} g/(cms)$, $\mu_g = 1.77 \times 10^{-4} g/(cms)$, $\rho_l = 1.0 g/cm^3$, $\rho_g = 0.001225 g/cm^3$, and $\gamma = 72.8 dynes/cm$. In our computations we use dimensionless parameters where the Reynolds number $R = \rho_l LU/\mu_l$ is 7.5, the Weber number $W = \rho_l LU^2/\gamma$ is 1, $L = 1$ micron, $U = 8.53 m/s$ and the density and viscosity ratios are 816 and 64 respectively.

In Figure 1, we display the results of our computations for the capillary jet as it breaks up. In Tables 1 and 2, we measure the relative errors for the interface and velocity field for grid resolutions ranging from 32x64 to 128x256. As shown by the tables, we obtain about first order accuracy before ($t = 80$) and after ($t = 120$) pinch off. We have only first order accuracy for this problem because of the density and viscosity jump across the interface. For example, when we recomputed the capillary jet problem with constant density $\rho_l = \rho_g = 1.0 g/cm^3$ and constant viscosity $\mu_l = \mu_g = 1.138 \times 10^{-2} g/(cms)$ the relative errors for the recomputed problem, shown in Tables 3 (before pinch-off) and 4 (after pinch-off), clearly show second order convergence.

6 AXISYMMETRIC JETTING CONVERGENCE STUDY

In this section, we present a numerical convergence study for a micro-scale jetting problem. In Figure 2 we display results using adaptive mesh refinement (Sussman et al., 1999) where the effective fine grid resolution is 64x1024. The diameter of the nozzle is 32 microns and the length of the nozzle is 70 microns. In Figure 3 we display the pressure profile that is applied at the base of the nozzle. This particular pressure impulse models the effect of a piezo-electric jetting device. In Table 5 we display the relative errors

Table 2. Convergence study using the CLS algorithm for the capillary instability problem. All data in terms of dimensionless parameters. $t = 120.0$, $\mu_l/\mu_g = 64$, $\rho_l/\rho_g = 816$.

grid	E(interface)	$E_{u,L1}$	$E_{u,\max}$
16x32	N/A	N/A	N/A
32x64	318.9	936.2	0.90
64x128	182.9	599.3	1.32
128x256	76.8	150.6	0.53

Table 3. Convergence study using the CLS algorithm for the capillary instability problem. All data in terms of dimensionless parameters. $t = 120.0$, $\mu_l/\mu_g = 1$, $\rho_l/\rho_g = 1$.

grid	E(interface)	$E_{u,L1}$	$E_{u,\max}$
16x32	N/A	N/A	N/A
32x64	52.76	68.55	0.1535
64x128	11.23	16.17	0.0339
128x256	2.82	4.24	0.0091

Table 4. Convergence study using the CLS algorithm for the capillary instability problem. All data in terms of dimensionless parameters. $t = 160.0$, $\mu_l/\mu_g = 1$, $\rho_l/\rho_g = 1$.

grid	E(interface)	$E_{u,L1}$	$E_{u,\max}$
16x32	N/A	N/A	N/A
32x64	78.3	125.3	0.143
64x128	15.3	47.6	0.177
128x256	3.0	12.9	0.090

between computations in which we successively add finer resolved adaptive grids.

7 THREE DIMENSIONAL JETTING COMPUTATIONS

In this section, we display preliminary results of three-dimensional, adaptive ink-jet computations. Three dimensional computations are necessary for studying asymmetric effects that the geometry of the nozzle can have on the resultant ejected droplet(s). In figure 6, we display computations from a nozzle with a square base. The pressure impulse is applied at the base of the nozzle and is similar

Table 5. Convergence study using the CLS algorithm for the axisymmetric jetting of ink. $t = 70$ microseconds, $\mu_l/\mu_g = 64$, $\rho_l/\rho_g = 816$.

grid	E(interface)	$E_{u,L1}$
16x256	N/A	N/A
32x512	6.1E4	1.3E6
64x1024	2.7E4	5.5E5

to that displayed in figure 3. In figure 4, we display computations where the pressure impulse is applied from the side. The configuration here resembles the so called "side-shooter" geometries used for thermal ink-jet devices. The pressure impulse for a thermal ink-jet device models the growth and collapse of a vapor bubble at the "heater" of the nozzle. In figure 5 we plot the pressure impulse versus time for the side shooter computation.

8 CONCLUSION

We have developed a high order accurate numerical method for modeling jetting in micro-jet devices and have demonstrated that the method is second order accurate on problems with no jump and first order accurate on problems in which there is a discontinuity in density and viscosity at the interface.

REFERENCES

Bechtel, S., Carlson, C., and Forest, M. (1995). Recovery of the rayleigh capillary instability from slender 1d inviscid and viscous models. *Phys. Fluids*, 7 (12):2956–2971.

Bell, J. B., Colella, P., and Glaz, H. M. (1989). A second-order projection method for the incompressible Navier-Stokes equations. *J. Comput. Phys.*, 85:257–283.

Bell, J. B. and Marcus, D. L. (1992). A second-order projection method for variable-density flows. *J. Comp. Phys.*, 101:334–348.

Bernardini, G., Rampy, B., Howell, G., Hayes, D., and Frederickson, C. (1991). Applications of piezoelectric fluid jetting devices to neuroscience research. *J. Neuroscience Methods*, 38:81–88.

Chang, Y., Hou, T., Merriman, B., and Osher, S. (1996). Eulerian capturing methods based on a level set formulation for incompressible fluid interfaces. *J. Comp. Phys.*, 124:449–464.

Hayes, D., Wallace, D., Boldman, M., and Marusak, R. (1993). Picoliter solder droplet dispensing. *Inter. J. Microcircuits and Electronic Packaging*, 16:173–180.

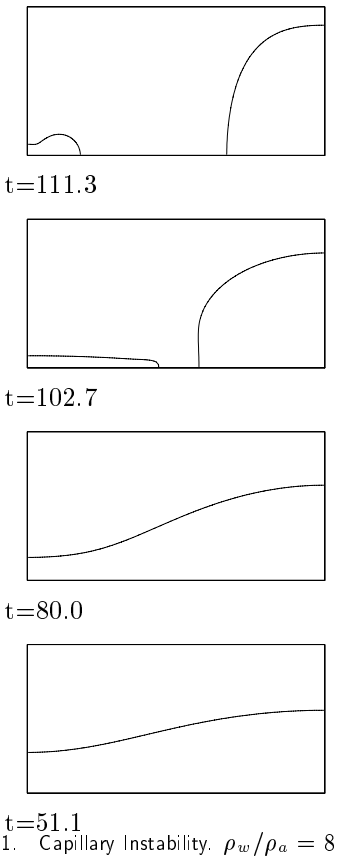

Figure 1. Capillary Instability. $\rho_w/\rho_a = 816$, $\mu_w/\mu_a = 64$. Grid resolution is 64x128.

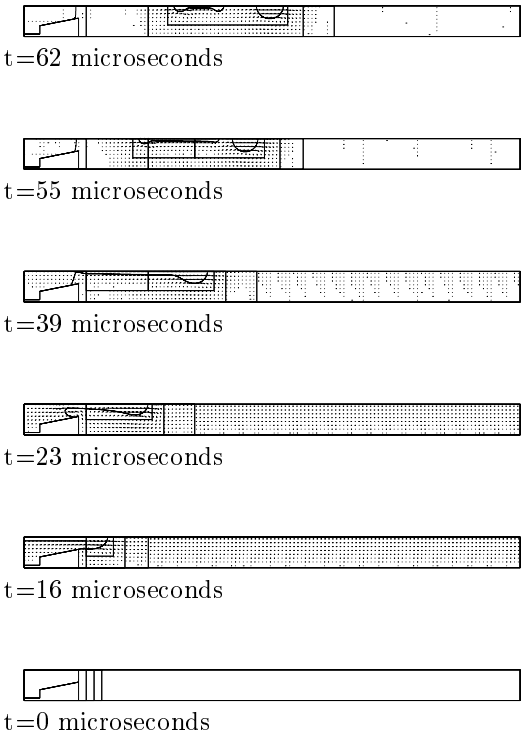

Figure 2. Axisymmetric jetting of ink. $\rho_w/\rho_a = 816$, $\mu_w/\mu_a = 64$. Effective fine grid resolution is 64x1024.

Rayleigh, L. (1878). On the instability of jets. *Proceedings of the London Mathematical Society*, 10(4).

Sussman, M., Almgren, A., Bell, J., Colella, P., Howell, L., and Welcome, M. (1999). An adaptive level set approach for incompressible two-phase flows. *J. Comp. Phys.*, 148:81–124.

Sussman, M. and Puckett, E. (1998). A coupled level set and volume of fluid method for computing 3d and and axisymmetric incompressible two-phase flows. *J. Comp. Phys.* submitted.

Sussman, M., Smereka, P., and Osher, S. (1994). A level set approach for computing solutions to incompressible two-phase flow. *J. Comp. Phys.*, 114:146–159.

Wallace, D., Hayes, D., Frederickson, C., and Howell, G. (1989). The application of ink-jet technology to neuroscience research and biomedical research. Bioprocess Engineering Symposium, Diller TE, Hochmuth RM, Cho YI (ed.), The American Society of Mechanical Engineers (H00579).

Wallace, D. B. (1993). Capillary instability of a jet of liquid metal. *Journal of Fluids Engineering*, 115:529–532.

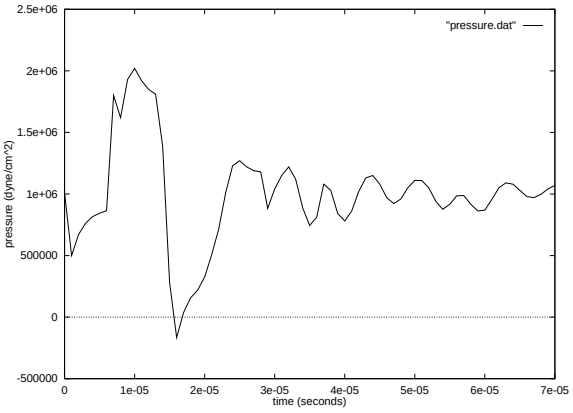

Figure 3. Pressure versus time applied to base of nozzle for modeling piezoelectric device.

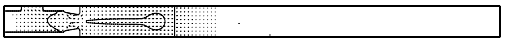

t=11 microseconds (y-z slice)

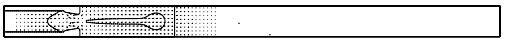

t=11 microseconds (x-z slice)

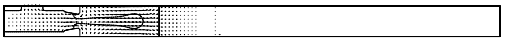

t=9 microseconds (y-z slice)

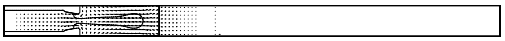

t=9 microseconds (x-z slice)

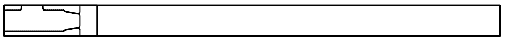

t=0 microseconds (y-z slice)

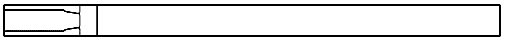

t=0 microseconds (x-z slice)

Figure 4. 3d computation of jetting of ink for "side shooter" geometry. $\rho_w/\rho_a = 816$, $\mu_w/\mu_a = 64$. Effective fine grid resolution is 16x16x256.

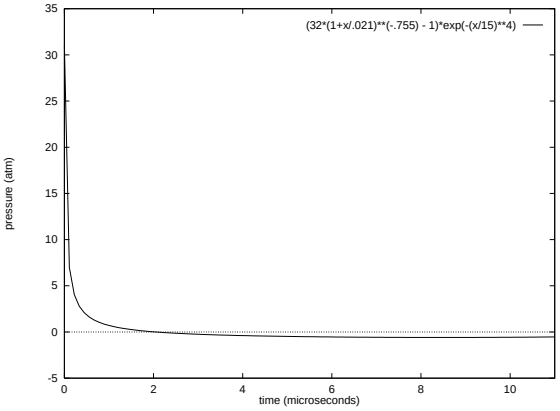

Figure 5. Pressure versus time applied to side of nozzle for modeling thermal ink-jet device.

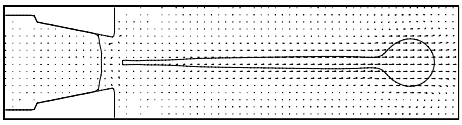

t=42 microseconds (y-z slice)

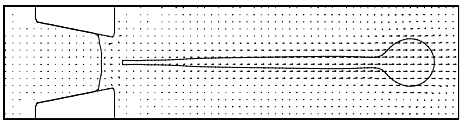

t=42 microseconds (x-z slice)

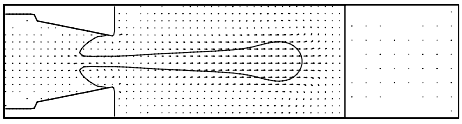

t=26 microseconds (y-z slice)

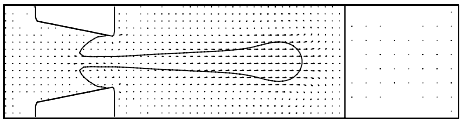

t=26 microseconds (x-z slice)

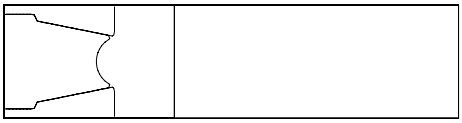

t=0 microseconds (y-z slice)

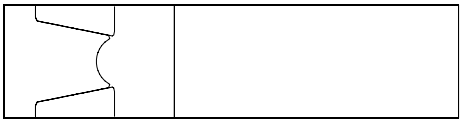

t=0 microseconds (x-z slice)

Figure 6. 3d computation of jetting of ink. $\rho_w/\rho_a = 816$, $\mu_w/\mu_a = 64$. Effective fine grid resolution is 32x32x128.